Journal of Aerosol Science 194 (2026) 106786

Contents lists available at ScienceDirect

Journal of Aerosol Science

journal homepage: www.elsevier.com/locate/jaerosci

Role of soot particle properties and activation in contrail formation using LES with online-coupled microphysics

Parisa Afkari *, Mohamed Chouak, Sébastien Cantin, François Garnier

Aero Propulsion Laboratory, Aerospace Engineering Department, École de technologie supérieure, University of Quebec, Montreal, Canada

ARTICLE INFO

Keywords:
Contrails
Activation
Soot particle
Microphysics
Water activity
Hygroscopicity parameter

ABSTRACT

Aircraft contrails form through ice crystal nucleation initiated primarily by engine-emitted particles. These ice crystals can lead to persistent contrails, contributing to climate warming, thus making understanding their activation a key target for mitigation strategies. This study presents large eddy simulations (LES) coupled with a refined soot activation model. The microphysical scheme incorporates solute effects through the hygroscopicity parameter (κ), enabling a more realistic representation of water activity during soot particle activation. These numerical simulations utilized a LEAP-1A engine under realistic cruise conditions, examining three scenarios: (i) varying κ (0.0005, 0.005, 0.0142), corresponding to an equivalent fuel sulfur content (FSC) of 50, 410, and 1270 ppm, respectively; (ii) varying initial soot emission indices (10^{13}–10^{15} #/kg-fuel), and (iii) varying initial soot core radii (10–30 nm). The results indicated that reducing κ from 0.0142 to 0.0005 slightly reduced ice particle radii, yet increased the activation fraction by ~20% due to enhanced water vapor availability. Reducing the initial soot number in two successive steps, from 10^{15} to 10^{13} #/kg-fuel, increased the mean ice particle radius from ~0.3 μm to 2.4 μm in 1 s and elevated the activated fraction by ~66%. Larger initial soot core radii enhanced activation by ~20%, with mean ice particle radius differences reaching ~80% in around 0.4 s and narrowing to ~10% by 1s. Additionally, the results highlighted the importance of 3D LES with online-coupled microphysics, whereas the 0D offline box model overpredicted activation more than 50% and misrepresented the κ sensitivity.

1. Introduction

An initial contrail forms when moist exhaust mixes with cold ambient air. Depending on surrounding atmospheric conditions, it can be short- or long-lived, spreading and increasing cloudiness and affecting Earth's radiation balance (IATA, 2024; Kärcher, 2018). Mitigating contrail impacts requires both comprehensive data and improved models, which allow to evaluate possible trade-offs between alternative strategies. Recent advances in measurements and modeling now allow contrail formation to be investigated at smaller scales, bridging detailed process-level studies and large-scale models (Kärcher, 2018).

The dynamics of the exhaust plume, together with ambient atmospheric conditions, are among the key factors influencing near-field contrail formation (Paoli et al., 2013). However, uncertainties remain about how the mixing of the aircraft engine exhaust plume with ambient air affects microphysical processes during contrail development. Addressing this gap is crucial, as mixing can control initial ice-crystal properties, influencing contrail evolution under given ambient conditions (Singh et al., 2024). Early

* Corresponding author.
E-mail address: parisa.afkari.1@ens.etsmtl.ca (P. Afkari).

https://doi.org/10.1016/j.jaerosci.2026.106786
Received 3 September 2025; Received in revised form 18 March 2026; Accepted 23 March 2026
Available online 24 March 2026

evaluations of plume mixing lines began with the Schmidt-Appleman criterion, which established the fundamental conditions for contrail formation and threshold temperatures (Appleman, 1953; Schmidt, 1941). Schumann (Schumann, 1996) later refined this framework by defining the slope of the mixing line based on engine parameters. However, jet plume mixing and cooling are more complex processes, influencing the evolution of individual exhaust particles while preserving their unique physical properties throughout plume development. A detailed examination of mixing processes under diverse conditions poses challenges in experimental campaigns, underscoring the role of numerical studies in providing comprehensive insights. To incorporate additional physical processes, three-dimensional (3D) simulations resolve plume dynamics using turbulence modeling (Lewellen, 2020), capturing the inhomogeneity of plume mixing in the radial directions. In contrast, zero-dimensional (0D) mixing models simplify plume dynamics through parameterized or plume-averaged mixing (Kärcher et al., 2015). In recent decades, numerous numerical studies have contributed to understanding the dynamics and mixing processes in the jet and vortex phases of contrail formation. For example, Khou et al. (Khou et al., 2015) conducted 3D simulations to investigate early contrail development in the near-field of a realistic commercial aircraft, focusing on mixing processes in the bulk plume and achieving alignment with experimental data.

Accurately predicting contrail properties requires coupling exhaust plume mixing dynamics with microphysical processes. Such coupling occurs either through online integration within each time step, enabling real-time interactions, or through offline sequential processing once plume dynamics have been computed. To add complexity while managing computational costs, some studies, such as Paoli et al. (Paoli et al., 2008), opted for offline microphysical modeling. However, for improved accuracy, studies like Khou et al. (Khou et al., 2017) utilized 3D online Reynolds-Averaged Navier-Stokes (RANS) coupling with an Eulerian approach for ice particle growth, capturing detailed interactions in contrail formation. Furthermore, Lewellen (Lewellen, 2020) ran large eddy simulations (LES) of the exhaust plume and bin-resolved Eulerian microphysics, and then initialized the offline wake/vortex stage from a pre-computed 2D RANS wake field. Subsequently, Bier et al. (Bier et al., 2022) conducted a Lagrangian particle microphysics box model (LCM) offline along trajectory ensembles extracted from a FludiLES 3D LES and compared it against Lewellen's 3D LES (Lewellen, 2020) with online microphysics. The offline ensemble yielded a higher ice emission index (EI_{ice}) because inter-parcel mixing in the full 3D LES suppresses subsequent activation—an interaction absent from the offline ensemble. Vancassel et al. (Vancassel et al., 2014) also noted that the online approach provided immediate feedback and improved the accuracy of dynamic growth and ice formation predictions as compared to the offline approach.

Aircraft engine exhaust releases a complex mixture of emissions that contribute to contrail formation, either directly, as condensation nuclei, or indirectly, through chemical reactions that enhance the process. Soot particles can play a major role in the exhaust plume, particularly under soot-rich conditions, by competing with liquid plume particles and ambient aerosols for the formation of contrail ice particles (Kärcher et al., 2009). However, soot particles are inherently hydrophobic (Popovicheva et al., 2008). A portion of the fuel sulfur in the exhaust plume is converted into sulfuric acid, which condenses onto the soot surfaces, enhancing their hygroscopicity and promoting water uptake through heterogeneous nucleation (Schumann et al., 1996). Thus, the presence of sulfuric acid influences aircraft exhaust composition and contrail formation. Schumann et al. (Schumann et al., 2002), as part of SULFUR experiments (SULFUR 1–7), demonstrated that at a fuel sulfur content (FSC) greater than 100 ppm, sulfuric acid becomes the dominant precursor for volatile aerosols, with conversion fractions of 0.34–4.5% for older engines and approximately $3.3 \pm 1.8\%$ for modern engines. The number of contrail ice particles correlated strongly with the soot particle number at lower sulfur contents, but became increasingly dependent on the fuel sulfur content as the FSC increased. Additionally, as Yu et al. (Yu et al., 2024) indicated, the activation of nonvolatile soot particles during contrail formation is primarily influenced by the primary soot particle size, rather than the soot aggregate size, which accounts for the lower-than-expected fraction of soot particles forming ice. The authors also acknowledged large uncertainties regarding the contribution of volatile particles, particularly due to the unaccounted role of organic species in nucleation and growth. However, they noted that under soot-poor and low-FSC conditions, as well as in soot-rich regimes, the influence of volatile particles on ice formation is limited. On the other hand, reducing soot number emissions, the primary factor controlling ice particle formation in contrails, remains a key area of interest, with numerous campaigns evaluating different strategies. Mitigation approaches, such as using alternative fuel blends with lower aromatic content, are particularly relevant for this purpose (Bräuer et al., 2021; Voigt et al., 2021).

Beyond particle type, incorporating soot particle activation in theoretical and numerical studies provides the basis for activation theory in contrail microphysics. Petzold et al. (Petzold et al., 2005) experimentally investigated how the fuel sulfur content affects the Cloud Condensation Nuclei (CCN) activation of soot, interpreting measurements with classical Köhler theory. They concluded that a higher FSC (via increased sulfuric acid (H_2SO_4) and sulfate coating) increases the soluble fraction and decreases the activation diameter (i.e., lowers the critical supersaturation). Subsequently, Petters and Kreidenweis (Petters et al., 2007) introduced a method to describe the relationship between the aerosol particle dry diameter and CCN activity using a single hygroscopicity parameter (κ). They provided hygroscopicity values ranging from highly soluble to non-hygroscopic components. The model effectively predicts CCN activity for mixed particles, including those containing surface-active materials, with results agreeing within uncertainties of measured values. The κ-Köhler activation method has thus been used in several numerical studies and modeling efforts, such as those by Lewellen (Lewellen, 2020), Bier et al. (Bier et al., 2022) and Yu et al. (Yu et al., 2024). However, in each of these cases, including challenges remained in modeling, particularly with respect to the coupling strategy and the representation of fully 3D mixing.

As such, this study aims to integrate the κ-Köhler theoretical model into an online-coupled microphysical model within the FludiLES high-order LES code. It focuses on the activation of soot particles within 1s of plume age under different κ, simulating different levels of FSC, as well as varying initial soot number emission indices (EI_{soot}) and initial dry soot core radii. To the authors' knowledge, no prior study has numerically evaluated these scenarios while simultaneously coupling soot particle activation online with the 3D plume dynamics.

The paper is structured as follows: Section 2 details the numerical methodology adopted, covering both the dynamic and

microphysical models. Section 3 presents the parametric microphysical analysis in four subsections. The first examines the effect of fuel sulfur content. The second investigates initial soot number emission indices, and the third explores variations in the initial dry soot core radius. Lastly, the fourth subsection compares a 0D offline box model with 3D LES with online-coupled microphysics to evaluate how explicitly resolving plume dynamics influences microphysics.

2. Numerical methodology

The modeling approach simulates an exhaust jet, with a gas phase (air and water vapor) containing soot particles from the core flow. The exhausted particles compete for activation, leading to ice particle formation within the plume. This section presents the mathematical framework for the flow dynamics of the jet gas phase, followed by solid phase modeling for soot particles and their microphysical pathways in contrail formation.

2.1. Dynamic flow model

Jet flow is simulated using an Eulerian-based temporal LES approach with a high-order compressible computational fluid dynamic (CFD) code, FludiLES. The 3D Navier-Stokes equations for the gas-flow mixture and the numerical setup in FludiLES were detailed in Afkari et al. (Afkari et al., 2025). The LES method filters large-scale turbulence while modeling smaller scales using a subgrid-scale hybrid Smagorinsky model. Given the low mass ratio between the solid phase (soot, ambient, and ice particles) and the gas phase (air and water vapor mixture), no coupling terms are included in the continuity and momentum equations. Thermal exchanges from ice particles to the gas phase are included in the energy equation, as latent heat release from ice particle growth modifies the local temperature field and contributes to thermal coupling. However, in the present young-plume simulations, this latent-heating feedback is neglected because the particle mass loading is small and the associated thermal coupling is weak. Furthermore, mass exchange is included via the mass transfer term, where the source term in the water vapor mass fraction conservation equation represents the condensation rate, calculated using an ice particle growth model detailed in the microphysical section (Section 2.2). This research code, based on the finite-difference scheme with spectral-like resolution, has been extensively used and validated for engine jet and aircraft wake applications (Brunet et al., 1999; Gago et al., 2002, 2003; Garnier et al., 1997, 2003, 2014; Labbe et al., 2007; Vancassel et al., 2014).

A Cartesian frame (x, y, z) is used with y the streamwise (jet-axis) direction; the radial distance is $r = \sqrt{x^2 + z^2}$, so inlet profiles are prescribed as $U(r)$ and $T(r)$. The velocity field ($U(r)$) is initialized as the sum of two hyperbolic tangent profiles, based on the core and bypass jet flow parameters described in Afkari et al. (Afkari et al., 2025). The initial temperature profile is obtained using the Crocco-Busemann relation, whose validity has been numerically verified for jet flow (Panda et al., 2004). To initiate the development of turbulent phenomena, low-amplitude pseudo-random perturbations, weighted by a Gaussian profile and centered at the jet half-width radius, are added to the velocity components, such that:

$$u'_{x,z} = A \times f \times \left(exp\left\{ - \left[\frac{1}{4} \frac{R}{\theta} \left(\frac{r}{R} - \frac{R}{r} \right) \right]^2 \right\} \right)^{1/2} \tag{1}$$

$$u'_{y} = A \times f \times \left(0.95\, exp\left\{ - \left[\frac{1}{4} \frac{R}{\theta} \left(\frac{r}{R} - \frac{R}{r} \right) \right]^2 \right\} + 0.05(1 - U(r)) \right)^{1/2} \tag{2}$$

The terms $u'_{x,z}$ represent the transverse velocity components, and u'_{y} represents the velocity component in the flow direction. Here, θ denotes the boundary layer thickness of the jet shear layer, R defines the center of the jet shear layer, A represents the amplitude of the perturbations. With this formulation, the resulting nozzle-exit turbulence intensity is $TI(r) = u'_{\mathrm{rms}}(r)/U_{\mathrm{ref}}$ and scales approximately as $TI(r) \approx A\, \sigma_f\, G_n(r)$, where $\sigma_f = \mathrm{RMS}\{\mathrm{filtered}\, f\}$; therefore, A directly sets the imposed TI level. A sensitivity study of the perturbation amplitude was performed for three values of A, showing noticeable changes from 1% to 5%, while the results were nearly converged between 5% and 10%; therefore, $A = 5\%$ was retained as the baseline. Furthermore, f is a pseudo-random function generated by the *random_number* subroutine.

Table 1
Input parameters for dynamic simulations of LEAP-1A engine.

Parameters	Values
Core velocity, U_c (m.s^{-1})	400
Bypass velocity, U_b (m.s^{-1})	306
Bypass static temperature, T_b (K)	233
Core static temperature, T_c (K)	580
Molar fraction of jet core water vapor, $X_{(H_2O)_{v-jet}}$	0.0394
Cruise altitude (ft)	35000
Ambient temperature (K)	218.8
Ice relative humidity	110%
Molar fraction of ambient water vapor, $X_{(H_2O)_{v-\infty}}$	10.5 10^{-5}

$$f = 2 \times random\_number - 1 \quad (3)$$

f depends on each point in space and spans the [−1; 1] interval. It should be noted that the values taken by f for each velocity component are, a priori, different and uncorrelated.

A realistic LEAP-1A engine at cruise conditions is considered under a supersaturation ambient condition, followed by a detailed microphysical study, which is presented in the next section. The engine parameters considered for the dynamic simulation are summarized in Table 1 (Afkari et al., 2025).

In order to discretize the convective terms in the equations of continuity, momentum, and energy, a compact scheme of order 6 is used (Lele, 1992). Aside from being accurate in terms of truncation error, this scheme is also highly precise in terms of pseudo-spectral accuracy (dispersive error) over a wide range of scales. This resolution is quantified from a Fourier analysis described by Vichnevetsky and Bowles (Vichnevetsky et al., 1982). Also, the dissipation terms are discretized by second-order centered schemes. Time discretization is performed using a compact three-step Runge-Kutta scheme. This scheme is third-order accurate, and requires only two storage arrays per variable (DeVries et al., 2011).

The temporal domain is discretized on a structured Cartesian grid of 141 × 82 × 141 nodes, corresponding to a uniform resolution of size Δx = Δy = Δz = 0.15R, with a maximum Courant number of 0.6. Grid errors were further evaluated using the Grid Convergence Index (GCI) method proposed by Celik et al. (Celik et al., 2008), based on three meshes defined over the same domain: a coarse mesh of 106 × 62 × 106 nodes ($\Delta x = \Delta y = \Delta z = 0.20R$), the medium (baseline) mesh of 141 × 82 × 141 nodes ($\Delta x = \Delta y = \Delta z = 0.15R$), and a fine mesh of 211 × 122 × 211 nodes ($\Delta x = \Delta y = \Delta z = 0.10R$). The analysis, based on axial velocity within the mixing layer, resulted in $GCI^{23}_{fine} \approx 0.21\%$ and $GCI^{12}_{coarse} \approx 0.45\%$; for temperature, the corresponding indices were $GCI^{23}_{fine} \approx 0.34\%$ and $GCI^{12}_{coarse} \approx 0.41\%$, indicating discretization uncertainties below 1% on the medium grid for both quantities.

The initial configuration of the computational domain is depicted in Fig. 1, showing the temperature initialization on an x-slice plane along with the soot particles distributions. The spatial coordinates are reported in non-dimensional form using R ($x = \frac{L_x}{R} = 21$, $y = \frac{L_y}{R} = 12$, and $z = \frac{L_z}{R} = 21$). Following Paoli and Garnier (Paoli et al., 2005), the streamwise domain length was chosen to exceed the wavelength of the most amplified first azimuthal instability, leading here to $L_y = 2\lambda = 12R$. To further verify this choice, the microphysical results obtained with the longer domain $(L_y = 18R)$ were compared with those of the baseline case $(L_y = 12R)$, and both showed nearly the same temporal evolution, with deviations remaining below 10%.

In a temporal jet LES, the streamwise direction is treated with periodic boundary conditions, so the computational domain represents a locally parallel jet segment without physical inflow or outflow planes. The flow is initialized at $t = 0$ with the prescribed mean core/bypass profiles (velocity and temperature), the surrounding ambient, and low-amplitude perturbations to trigger shear-layer instability. The simulation is then advanced in time; Kelvin–Helmholtz roll-up, transition, and fully developed turbulence arise naturally, leading to radial spreading, entrainment of ambient air, and decay of centerline velocity/temperature. Non-reflective boundary conditions are imposed on the remaining surfaces, and a sponge zone (9-cell-thick sponge layer) is introduced to dampen turbulent fluctuations using a smoothly ramped relaxation term (Maglaras, 2007).

2.2. Microphysical model

The microphysical model in this study builds upon the framework established in Afkari et al. (Afkari et al., 2025), incorporating an improved activation method for each soot particle and accounting for the solute effects of the fuel sulfur content by modeling water

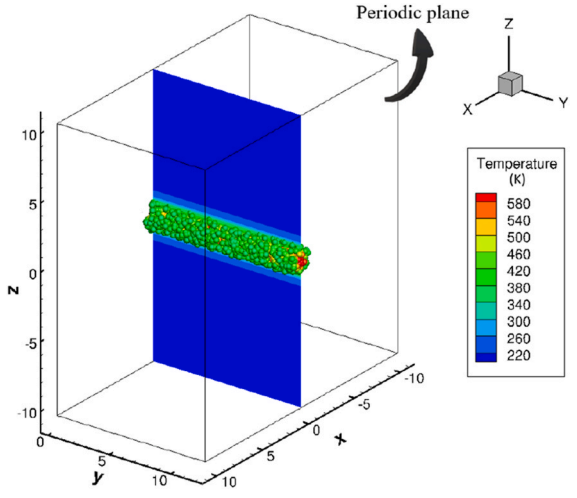

Fig. 1. Initial state of the computational domain at time zero, showing the temperature distribution on an x-slice plane and the initialized soot particles. The inlet and periodic boundary planes are indicated, defining the domain's flow conditions.

activity through the hygroscopicity parameter (κ). In the modeling framework, numerical particles each represent a packet of physical particles.

Based on the κ-Köhler theory introduced by Petters and Kreidenweis (Petters et al., 2007), the equilibrium saturation ratio over a droplet or ice crystal surface can be expressed using **Eq. (4)**. This equilibrium depends on the Kelvin effect (**Eq. (5)**), the water activity in the droplet solution, α_w and the droplet radius:

$$Ke = \frac{2\sigma_w M_{H_2O}}{RT_p\rho_p} \tag{4}$$

$$S_k = \alpha_w.\exp\left(\frac{Ke}{r_p}\right) = \frac{{r_p}^3 - {r_d}^3}{{r_p}^3 - {r_d}^3(1-\kappa)}\exp\left(\frac{Ke}{r_p}\right) \tag{5}$$

where r_p represents the droplet radius and r_d denotes the initial dry core radius of soot particles.

On the other hand, the actual saturation ratio of water vapor, S_w, is determined based on the local available water vapor content in the environment, which varies due to the mixing between the jet plume and the ambient atmosphere. It is defined as:

$$S_w = \frac{P_{H_2O,actual}}{P_{sat}(T_P)} \tag{6}$$

where P_{sat} is the saturation vapor pressure at particle temperature, T_P, computed based on the equations provided by Murphy and Koop (Murphy et al., 2005). S_w uses a phase-dependent P_{sat} (water for droplets, ice for ice particles) and $P_{H_2O,actual}$ is the partial pressure of available water vapor determined by the mole fraction of water vapor, X_v, in the environment and the local atmospheric pressure, P:

$$P_{H_2O,actual} = X_v \times P \tag{7}$$

The mole fraction X_v depends on the water vapor mass fraction, Y_v, and the ratio of molar masses of water vapor (M_{H_2O}) and dry air M_{Air}. Since mass fractions are typically more accessible in atmospheric modeling, the molar fraction is obtained by:

$$X_v = \frac{Y_v}{Y_v + (1 - Y_{mix}).\frac{M_{H_2O}}{M_{Air}}} \tag{8}$$

The mass fraction Y_v reflects the mixing between the ambient air and the jet plume, and varies spatially based on the degree of dilution between these two sources. The governing equation can therefore be written as:

$$Y_v = \mathscr{D}\left(Y_{v,j} - Y_{v,a}\right) + Y_{v,a} \tag{9}$$

where $\mathscr{D}$ is the plume dilution factor, which equals 1 at the jet exhaust and decreases toward 0 as the ambient entrainment dominates. $Y_{v,j}$ is the water vapor mass fraction of the jet exhaust, and $Y_{v,a}$ is the water vapor mass fraction of the ambient atmosphere.

The initial water vapor content of the ambient air and the jet plume are prescribed based on their respective mole fractions and the molar mass ratio of water vapor to dry air. So, each particle in the microphysical model has its own equilibrium saturation ratio, S_k, which depends on its local properties. By applying the Fukuta-Walter model (Fukuta et al., 1970) for liquid droplets and ice particles growth and modifying its equilibrium saturation, which was previously based solely on the Kelvin effect, the equation can be expressed as follows:

$$r_P\frac{dr_P}{dt} = \frac{S_w - S_k}{C_t S_k + C_P} \tag{10}$$

$$C_t = \frac{L^2 M_{H_2O}\rho_P}{k_g R\, T_P^2 f_{3\alpha}} \tag{11}$$

$$C_P = \frac{R\, T_P\rho_P}{P_{sat} D_\nu\, M_{H_2O} f_{3\beta}} \tag{12}$$

$$f_{3\alpha} = \frac{r_p}{r_p + \frac{k_g\sqrt{2\pi M_{Air}RT_P}}{\alpha P_\infty\left(C_{P,a} - R/2\right)}} \tag{13}$$

$$f_{3\beta} = \frac{r_p}{r_p + \frac{D_v}{\beta}\sqrt{\frac{2\pi M_v}{RT_P}}} \tag{14}$$

where C_t and C_P are factors related to condensed particle (liquid droplet or ice particle) growth and evaporation, and ρ_P represents the condensed-phase density, calculated using the correlation for water and ice phases as presented by Pruppacher (Pruppacher et al., 1979). The term $f_{3\alpha}$ is a correction factor that accounts for the temperature difference between the condensed particle and the surrounding air. P_∞ represents the fluid pressure in the region far from the condensed particle, beyond the boundary layer, where the influence of the condensed particle on the fluid flow is negligible. D_ν denotes the diffusivity of vapor in air, while L is the reference

length scale, also used in the calculation of the Reynolds number. $C_{P,a}$ refers to the specific heat capacity of air at constant pressure, R is the universal gas constant, and k_g represents the thermal conductivity of the gas.

The coefficient α (thermal accommodation coefficient) characterizes heat transfer at the interface between the gas and the condensed phase, and describes how effectively molecules exchange energy upon collision. In this study, α is set to 1, consistent with evidence of essentially complete thermal accommodation of $H_2O(g)$ on liquid water (Li et al., 2001). The parameter β represents the fraction of molecules that condense (or deposit) upon impacting the surface, commonly referred to as the condensation coefficient (or deposition coefficient, depending on the phase change). Although reported values of β range from 0.01 to 1, β is set to 1 here because water-vapor deposition on ice is close to unity at contrail-relevant low temperatures (Mozurkewich, 1986).

Furthermore, freezing is determined by the calculated freezing temperature for each activated droplet, as given by **Eq. (15)** (Kärcher et al., 2015):

$$T_* \cong \frac{1}{a_1}\left[\ln\left(\frac{a_1\dot{T}}{V_w}\right) - a_2\right] \tag{15}$$

where $a_1 = -3.5714\ (K^{-1})$ and $a_2 = 858.719$ are empirical constants (Riechers et al., 2013), $\dot{T}$ is the plume cooling rate, and V_w is the droplet volume.

Overall, the microphysical activation and growth strategy for aerosol particles begins with soot particles in their initial state as dry aerosols possessing a fixed core radius (r_d). Each particle experiences local environmental conditions, notably the saturation ratio (S_w). Since the equilibrium saturation ratio (S_k) depends on ice particle growth and starts off undefined, it is initialized considering only Kelvin effects. Activation occurs once the environmental saturation exceeds this threshold ($S_w > S_k$), triggering water condensation and marking the transition from a dry to a wet state. As the ice particle grows, even a slight increase in radius causes the water activity effects described by κ-Köhler theory to become more pronounced, decreasing the equilibrium saturation ratio below that predicted by the Kelvin effect alone; this reduction indeed indicates soot particle activation. Ice particle growth continues as long as the environmental saturation, linked to dynamic mixing, remains above the recalculated equilibrium saturation ratio ($S_w > S_k$), with the growth rate governed by diffusion-driven processes. If S_w falls below S_k, evaporation or sublimation may occur. However, ice particles are constrained from evaporating or sublimating to sizes smaller than their original dry core, thereby conserving the aerosol nucleus. Additionally, the strategy accounts for both liquid and ice phases by incorporating phase-specific properties such as surface tension, density, saturation vapor pressure, and the heat of vaporization or sublimation. Here, the particle's phase is determined by local temperature conditions, ensuring a comprehensive and physically realistic representation of aerosol particle evolution from activation through subsequent growth while maintaining numerical stability.

Initially, a scenario is investigated in which three different FSCs are analyzed at a soot emission index of $EI_{soot} \approx 10^{14}$/kg-fuel. This emission index was adopted to reflect the lean-burn design of the LEAP-1A (ICAO, 2024). Also, the initial dry soot core radius is fixed at 20 nm. Building on the experimentally established correlations between FSC and the soluble volume fraction (ε_{sol}) of sulfuric acid (Petzold et al., 2005), three distinct FSC levels are considered, as follows:

- Low FSC (50 ppm): $\varepsilon_{sol} < 0.1\%$
- Medium FSC (410 ppm): $0.8\% < \varepsilon_{sol} < 1.2\%$
- High FSC (1270 ppm): $2.7\% < \varepsilon_{sol} < 3\%$

For the effective κ, based on the work of Petters and Kreidenweis (Petters et al., 2007) on the hygroscopicity for mixed particles, where $\kappa = \sum_i \varepsilon_i \kappa_i$, it can be expressed as:

$$\kappa = \varepsilon_{sol} \times \kappa_{sol} + (1 - \varepsilon_{sol})\kappa_{insol} \tag{16}$$

where κ_{sol} and κ_{insol} denote the hygroscopicity parameter of the soluble and insoluble fractions, respectively. It is assumed that the contribution of each component to the overall hygroscopicity is proportional to its volume fraction. For soot particles coated with diluted sulfuric acid, κ_{sol} is taken as 0.5 (Kärcher et al., 2015), while κ_{insol} is considered 0, reflecting both the absence of the modeled insoluble material associated with the soot particle surface and its inherently insoluble, hydrophobic nature. When κ approaches 0, the particle becomes effectively hydrophobic, meaning it does not induce solute-driven water uptake or activate as a CCN. The water activity tends toward unity ($\alpha_w \approx 1$), corresponding to the wetting of the dry particle by a pure water film. It behaves as an insoluble but wettable particle, forming a thin water layer without significant uptake, following the Kelvin equation for vapor pressure over a curved surface (Petters et al., 2007). Consequently, the κ for soot particles under varying FSC conditions, calculated using **Eq. (16)**, is presented in Table 2.

To further assess the parametric study of the microphysical model, the effects of varying soot particle numbers are analyzed for a

Table 2
Hygroscopicity parameters (κ) for soot particles at varying FSC levels.

Fuel Sulfur Content Level	Soluble Volume Fraction of Sulfuric Acid	κ of Coated Soot Particles
50 ppm	$\varepsilon_{sol} \approx 0.1\%$	0.0005
410 ppm	$\varepsilon_{sol} \approx 1\%$	0.005
1270 ppm	$\varepsilon_{sol} \approx 2.85\%$	0.0142

low FSC content (50 ppm), which has the smallest κ for coated soot particles, with an initial dry soot core radius set at 20 nm. A low FSC level of 50 ppm is selected in a bid to minimize the contribution of volatile particle activation, which is not considered in this study, particularly in soot-poor regimes, as emphasized by Yu et al. (Yu et al., 2024). An analysis was conducted for the following soot number emission indices:

- Low soot number: $EI_{soot} \approx 10^{13}$ (kg-fuel)$^{-1}$
- Moderate soot number: $EI_{soot} \approx 10^{14}$ (kg-fuel)$^{-1}$
- High soot number: $EI_{soot} \approx 10^{15}$ (kg-fuel)$^{-1}$

Finally, in the last parametric study, the effects of the initial dry soot core radius are evaluated at a soot number emission index of $EI_{soot} \approx 10^{14}$/kg-fuel under a low FSC (50 ppm). The three selected dry core radii of soot particles are as follows:

- Small initial soot particles radius: $r_d = 10\ nm$
- Medium initial soot particles radius: $r_d = 20\ nm$
- Large initial soot particles radius: $r_d = 30\ nm$

Therefore, this integrated methodology ensures a comprehensive analysis by examining all three critical aspects of the behavior of the soot particles that may influence their activation and alter the microphysical pathway in contrail formation.

To compare 3D LES with online-coupled microphysics to a 0D offline box model for contrail formation, a temporal 3D LES without microphysics was conducted to isolate jet-phase mixing. A passive exhaust tracer defines the plume, and at each time step, the plume mean temperature $\overline{T}(t)$ and the plume mean dilution/entrainment rate $\overline{\omega}(t)$ are diagnosed from mass-weighted averages of the tracer and thermodynamic fields and saved on the LES time grid. These stored temperature and entrainment histories then drive the time-dependent 0D offline box model, which computes microphysical source terms for phase change mass transfer and latent heat. The box model employs the same κ-Köhler activation, condensational growth, sublimation, and freezing scheme as in the online-coupled microphysics configuration described in Afkari et al. (Afkari et al., 2025), and is solved offline. The gas-phase water vapor mass fraction and temperature evolve according to below equations (Riechers et al., 2013), driven by the $\overline{T}(t)$ and $\overline{\omega}(t)$ exported from the LES:

$$\dot{\overline{Y}}_v(t) = -\overline{\omega}(t)\left[\overline{Y}_v(t) - Y_{v,a}\right] + \xi_{PC}^{micro}(t) \tag{17}$$

$$\dot{\overline{T}}(t) = -\overline{\omega}(t)\left[\overline{T}(t) - T_a\right] + \xi_{LH}^{micro}(t) \tag{18}$$

where T_a is the ambient temperature and $\overline{Y}_v(t)$ is calculated from **Eq. (9)**, and the mean plume dilution factor $\overline{\mathscr{D}}$ (t) is obtained by integrating the LES-derived dilution rate $\overline{\omega}(t)$ over time. The microphysical source term ξ_{PC}^{micro} represents the phase-change mass

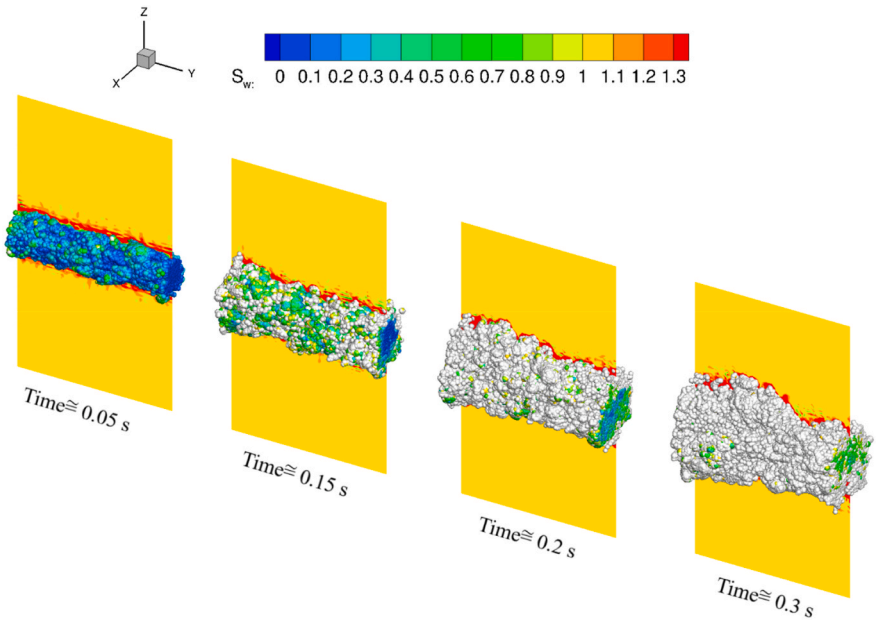

Fig. 2. Evolution of actual water saturation (S_w) over particles and on the central plane at different plume ages. Colored particles indicate the particles before activation, while white particles represent ice crystals.

transfer (negative for condensation, positive for sublimation) obtained from the κ-Köhler activation criterion using the soot dry core radius and κ, followed by diffusional growth; the thermal term ξ_{LH}^{micro} accounts for latent heat release or uptake. The total ice number and mass moments evolve under the same activation, growth, and freezing parameterizations as in the online model. The offline box carries no spatial coordinates and applies no feedback to the flow; rather, it integrates these equations in time on the LES time grid using the stored drivers.

3. Results analysis

3.1. Effect of particle hygroscopicity

The LEAP-1A engine with a fixed soot emission index of $EI_{soot} \approx 10^{14}$/kg-fuel and an initial dry soot core radius of 20 nm has been considered for three FSC levels – low (50 ppm), medium (410 ppm), and high (1270 ppm) – to analyze the effects of the FSC on the activation of soot particles.

Firstly, to visualize the 3D effects of jet microphysical properties, Fig. 2 presents the evolution of actual water saturation (S_w) over plume particles and along the central plane of the domain at various time steps, for a case with an initial $EI_{soot} \approx 10^{14}$/kg-fuel, an FSC of 410 ppm, and an initial dry soot core radius of 20 nm. As the jet mixes with ambient air, particles attain varying saturation levels, allowing uptake of ambient moisture. When the local saturation exceeds the particle equilibrium saturation, which occurs earlier for particles within the mixing region, droplet formation takes place. Over time, further cooling and supersaturation, particularly in regions of enhanced mixing, drive the transition from liquid droplets to ice crystals, shown as white particles.

Fig. 3 presents the temporal evolution of the mean actual saturation ratio ($\overline{S}_w$) and the mean equilibrium saturation ratio ($\overline{S}_k$), both calculated by averaging over all particles for three levels of fuel sulfur content: low, medium, and high, while maintaining a constant EI_{soot} of 10^{14}/kg-fuel and an initial dry soot core radius of 20 nm. At the initial stage, the actual saturation ratio increases as the jet cools and mixes with ambient air, reaching a peak corresponding to the maximum supersaturation, as shown in Fig. 3(a). A higher FSC (larger κ) facilitates soot activation at lower supersaturation levels, leading to earlier droplet growth. These early-formed droplets reduce vapor pressure, causing the supersaturation peak to occur sooner and at a lower magnitude. In contrast, a lower FSC delays activation, resulting in fewer activated particles in the early stages. This delay allows supersaturation to build to a higher peak and to remain elevated.

It should be noted that the equilibrium saturation ratio depends on the ice particle radius (as defined in **Eq. (5)**), and assigning the initial radius equal to the dry core radius yields an unrealistic value of zero. To address this, the Kelvin effect was incorporated at the start of the simulation, explaining the initial peak observed in Fig. 3(b). The curves show that different κ lead to variations in the equilibrium saturation. A higher FSC results in a lower equilibrium saturation, indicating a lower critical saturation required for activation. This is due to increased soot particle solubility, which enhances the water uptake and keeps the equilibrium saturation consistently lower than for medium and low fuel sulfur cases. The equilibrium supersaturations observed across different FSC levels in this study are consistent with the findings of Petzold et al. (Petzold et al., 2005), who reported that lower fuel sulfur reduces the soluble sulfuric acid coating on soot, thereby increasing the equilibrium or critical saturations required for activation, whereas a higher FSC increases the soluble fraction and decreases the equilibrium saturation.

To examine the influence of the FSC on microphysical properties, Fig. 4 illustrates its impact on soot particle growth and on the overall activation/freezing fraction, under a constant EI_{soot} of 10^{14}/kg-fuel and an initial dry soot core radius of 20 nm. Once activation

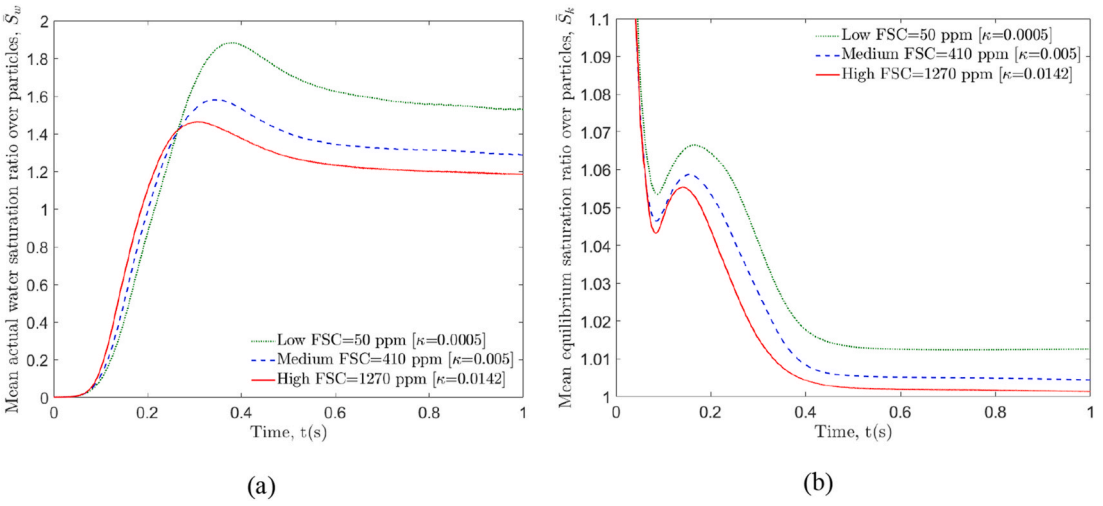

Fig. 3. Temporal evolution of (a) mean actual saturation ratio and (b) mean equilibrium saturation ratio for three FSC levels: low FSC = 50 ppm, medium FSC = 410 ppm, and high FSC = 1270 ppm, with a fixed EI_{soot} of 10^{14}/kg-fuel and an initial dry soot core radius of 20 nm.

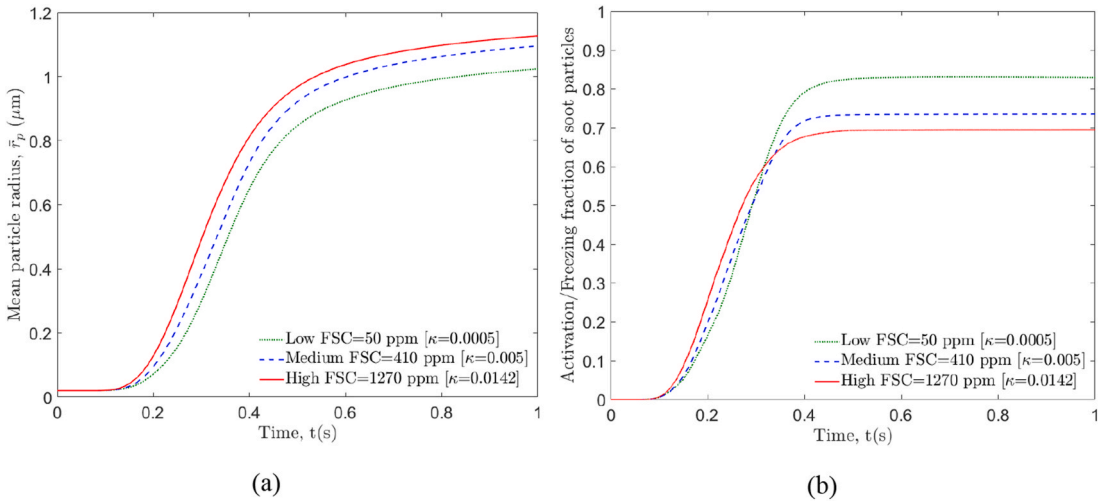

Fig. 4. Temporal evolution of (a) mean soot particle radius and (b) activation/freezing fraction of soot particles for three FSC levels: low FSC = 50 ppm, medium FSC = 410 ppm, and high FSC = 1270 ppm, with a fixed EI_{soot} of 10^{14}/kg-fuel and an initial dry soot core radius of 20 nm.

begins ($S_w > S_k$) for each soot particle, the mean radius increases rapidly as these particles absorb water and grow into droplets (see Fig. 4(a)). In Fig. 4(b), a higher FSC facilitates earlier activation due to increased soot particle solubility, leading to faster initial growth of up to around 0.3 s and ultimately larger ice particle sizes, as shown in Fig. 4(a). In contrast, a lower FSC delays activation, resulting in a slower growth rate. In the high FSC case, early activation and rapid growth quickly deplete the available water vapor, which limits further activation and leads to a lower final activated fraction. Conversely, in the low FSC case, delayed activation allows supersaturation to reach a higher peak and persist longer, resulting in a final activation fraction approximately 20% higher than that in the high FSC case. A similar κ-dependent response, where lower FSC increases the ice-crystal number while producing smaller ice crystals, was also reported by Cantin et al. (Cantin et al., 2025), consistent with the nonlinear activation and supersaturation feedback described above. These trends are consistent with the saturation behavior presented in Fig. 3, highlighting the competition for activation driven by multiple interacting parameters.

The findings align with two cases presented by Yu et al. (Yu et al., 2024), who included both soot and volatile particle activation in

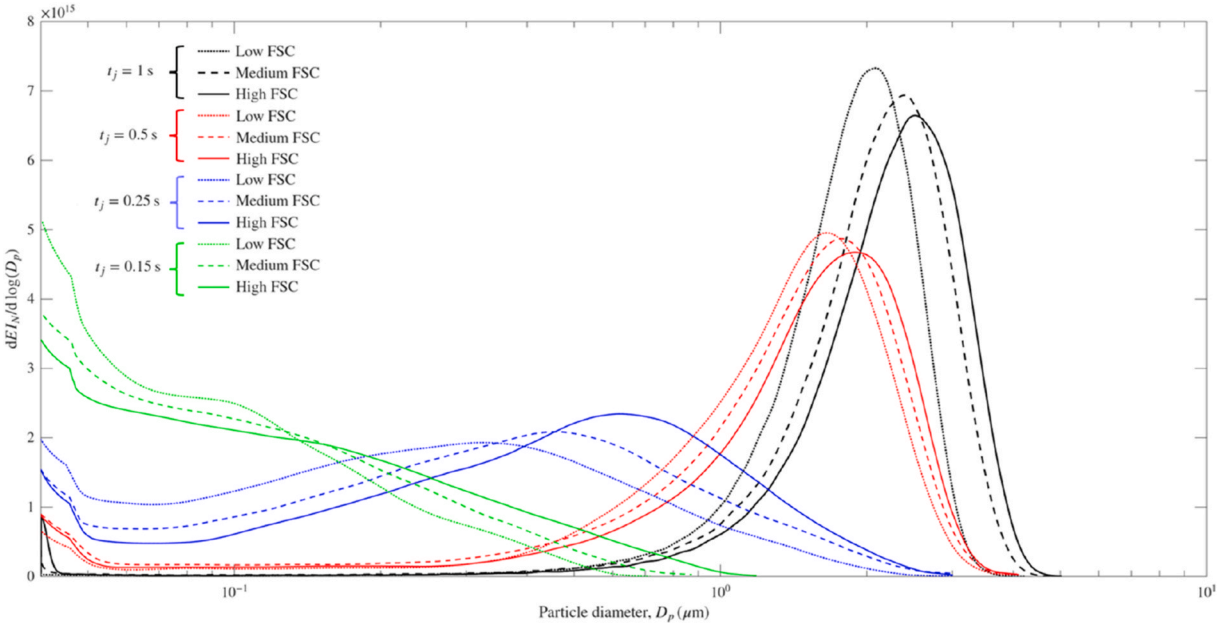

Fig. 5. Particle number emission index distribution $(dEI_N/d\log D_p)$ (1/kg-fuel) as a function of particle diameter for three FSC levels (low: 50 ppm, medium: 410 ppm, high: 1270 ppm) at plume ages $t_j = 0.15, 0.25, 0.5, 1$ s, with $EI_{soot} = 10^{14}$ (1/kg-fuel) and an initial dry soot core radius of 20 nm.

their microphysical model. Their results indicate that under nearly identical soot number emissions, the scenario with a lower fuel-sulfur content (FSC ≈ 70 ppm) exhibited a slightly higher soot-to-ice activation fraction as compared to the higher FSC scenario (FSC ≈ 570 ppm). However, this trend was not consistently observed across all their cases. The authors acknowledged large uncertainties arising from multiple controlling variables (e.g., RH_{ice}, temperature, particle size, and plume age), as well as additional complexities introduced by volatile particles and organic species.

To complement the mean quantities discussed above, Fig. 5 presents the time evolution of the particle number emission index distribution, $\left(dEI_N/d\log D_p\right)$, at plume ages $t_j = 0.15, 0.25, 0.5, 1$ s. The distributions provide a direct illustration of how activation proceeds under different hygroscopicity/FSC conditions. For higher hygroscopicity parameter, a larger fraction of ice particles shifts toward larger diameters at earlier times, indicating faster vapor uptake and explaining the reduced peak supersaturation and early plateau observed in the mean trends. In contrast, cases with stronger vapor limitation show that only part of the distribution shifts rapidly while the remainder stays near the small-diameter mode, providing distribution-level evidence for incomplete activation and the emergence of bimodal behavior.

3.2. Effect of initial soot emission number

This section analyzes three cases relating to the LEAP-1A engine, maintaining a fixed FSC level of 50 ppm (low) and an initial dry soot core radius of 20 nm. The study investigated three soot emission indices ($EI_{soot} \approx 10^{13}$, 10^{14}, and 10^{15}/kg-fuel) to assess the influence of the initial soot number on particle activation. Fig. 6 presents the temporal evolution of actual and equilibrium saturation ratios. At high EI_{soot} (10^{15}/kg-fuel), the large number of soot particles competing for available water vapor leads to rapid condensation, resulting in a lower peak supersaturation, followed by an almost immediate plateau, as shown in Fig. 6(a). This strong "condensational sink" prevents supersaturation from building up significantly. In contrast, at low EI_{soot} (10^{13}/kg-fuel), fewer droplets form, causing less immediate vapor depletion. This allows the actual saturation ratio to reach a higher peak and remain elevated for a longer period. The intermediate soot number case (10^{14}/kg-fuel) falls between these two trends. Conversely, as shown in Fig. 6(b), a higher EI_{soot} results in higher sustained equilibrium saturation ratios over time, thereby making soot activation more difficult. While several factors influence this behavior, at the same sulfur content, a greater number of soot particles increased the total surface area available for condensation. As a result, the system required a higher actual saturation ratio to exceed the equilibrium threshold for activation, thereby reducing the activation efficiency.

The temporal evolution of the mean particle radius (averaged over all particles, including soot and condensed ice) and the activation/freezing fraction for different EI_{soot} is presented in Fig. 7. As shown in Fig. 7(a), higher EI_{soot} lead to increased competition for water vapor, limiting individual particle growth and resulting in smaller mean radii. Conversely, lower EI_{soot} allow more water vapor per particle, promoting larger droplet growth. This trend is further reflected in Fig. 7(b), where stronger competition for water vapor at higher soot levels inhibits activation, yielding a lower final activation fraction of approximately 60 %. In contrast, lower soot cases support higher and more sustained supersaturation, leading to nearly full activation (up to 100 %) for 10^{13}/kg-fuel and an activation fraction of about 80 % for 10^{14}/kg-fuel. These findings follow the trend reported by Paoli et al. (Paoli et al., 2013), where higher EI_{soot} lowered the activated fraction from nearly complete activation at the lowest soot levels to roughly half at the highest levels. The absolute values are also consistent with those reported by Kärcher (Kärcher, 2016), particularly at EI_{soot} of 10^{14} and 10^{15}/kg-fuel for a plume age of 1s.

Fig. 8 presents the total (all-particle) number emission index distribution ($dEI_N/dlog(D_p)$ (1/kg-fuel)) as a function of particle diameter for different soot emission indices and FSC levels, with an initial dry soot core radius of 20 nm, at 1s plume age. All cases

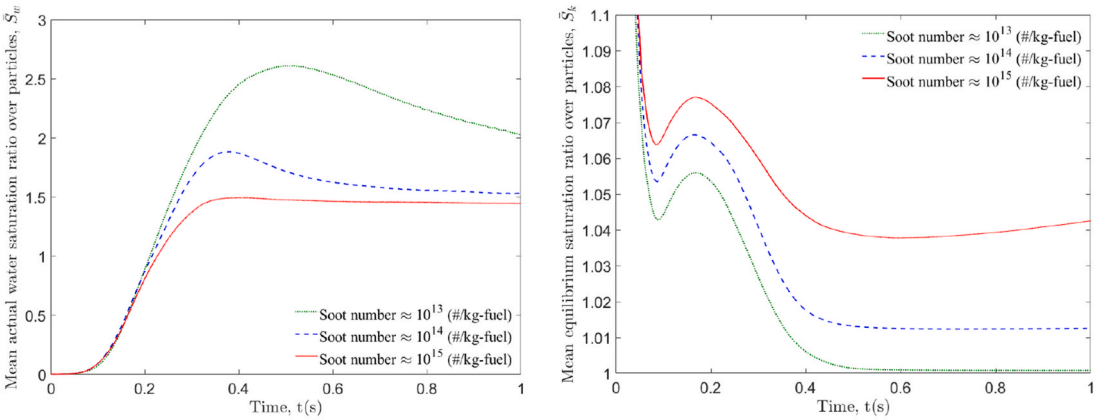

Fig. 6. Temporal evolution of (a) mean actual saturation ratio and (b) mean equilibrium saturation ratio for three EI_{soot} of 10^{13}, 10^{14}, and 10^{15}/kg-fuel at a fixed low FSC of 50 ppm and an initial dry soot core radius of 20 nm.

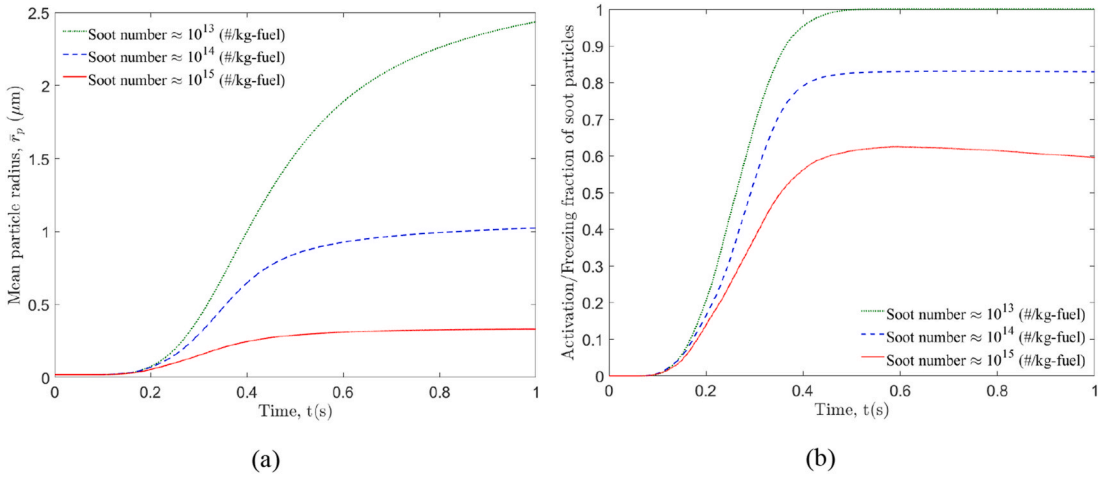

Fig. 7. Temporal evolution of (a) mean soot particle radius and (b) activation/freezing fraction of soot particles for three EI_{soot} of 10^{13}, 10^{14}, and 10^{15} (#/kg-fuel) at a fixed low FSC of 50 ppm and an initial dry soot core radius of 20 nm.

clearly demonstrate distinct peaks separated by FSC levels, with higher FSCs shifting the peak toward larger particle diameters, but at lower EI_{soot}, consistent with the results in Fig. 4. However, increasing the EI_{soot} from Fig. 8(a)–8(c) resulted in decreases differences between the FSC levels. Additionally, as the soot number increases, the particle distribution broadens and covers a wider range of diameters—a trend also reported by Wang & Miake-Lye (Wong et al., 2010). At $EI_{soot} \approx 10^{15}$/kg-fuel, the size spectrum thus becomes bimodal: a sub-100 nm mode of soot particles that never activate and a ~1 μm mode of fully activated ice crystals. The very large soot surface area reduces the available vapor, leaving a fraction unactivated and producing the twin peaks noted.

3.3. *Effect of initial dry soot core radius*

The influence of the initial dry soot core radius on particle saturation is shown in Fig. 9(a), where the peak in $\overline{S}_w$ occurs at different times, ranging from approximately 0.3 to 0.45s, starting with the largest initial dry radius of 30 nm. This is followed by a decline as water condenses onto particles and the plume dilution progresses. The results demonstrate that smaller dry soot particles (e.g., 10 nm) lead to a higher peak in $\overline{S}_w$, whereas larger soot particles (e.g., 30 nm) exhibit a lower peak. This behavior stems from the fact that larger soot particles experience a reduced Kelvin effect (i.e., lower equilibrium/critical supersaturation), and therefore activate earlier, thereby depleting the available supersaturation. In other words, the presence of larger soot cores enhances early vapor uptake and reduces the degree of supersaturation available for further growth. In contrast, smaller particles, with a lower individual condensation capacity, allow the plume to maintain a higher saturation ratio for a longer duration, thereby increasing the potential for additional particle activation and growth.

Smaller soot particles at 10 nm exhibit higher equilibrium saturation ratios $\overline{S}_k$, particularly in the early stages of plume evolution, as shown in Fig. 9(b). These particles require a higher ambient supersaturation to activate. In contrast, larger dry particles at 30 nm have lower equilibrium saturation ratios and can activate at lower supersaturation levels. Over time, $\overline{S}_k$ decreases as the plume cools, water condenses, and particles grow in size, which reduces the Kelvin effect and lowers the required equilibrium saturation. This behavior is consistent with what is observed by Petzold et al. (Petzold et al., 2005), who demonstrated that increasing the particle dry size and soluble sulfuric acid coatings reduce the critical supersaturation needed for soot activation.

The impact of the initial soot core radius on ice particle growth and activation is further illustrated in Fig. 10, using a soot emission index of $EI_{soot} \approx 10^{14}$/kg-fuel and a low FSC level of 50 ppm. As presented in Fig. 10(a), all cases exhibit rapid growth between approximately 0.2 and 0.6 s, driven by water vapor condensation in the supersaturated cooling plume. Larger initial soot particles (30 nm) grow more rapidly and reach a greater final size as compared to smaller ones (10 nm) within 1s. This is because larger soot particles can activate and condense water more easily, requiring lower ambient supersaturation, as previously shown in the equilibrium saturation results (Fig. 9(b)). Smaller soot particles experience delayed activation and slower growth due to their higher critical supersaturation requirements (Kelvin effect), which limits their ability to uptake water during the early stages. Furthermore, Fig. 10(b) shows the temporal evolution of the activation/freezing fraction of soot particles for different initial dry soot core radii (10, 20 and 30 nm). The results show that activation begins shortly and increases rapidly between 0.2 and 0.45s, coinciding with the peak in supersaturation (see Fig. 9(a)). Larger initial soot particles at 30 nm activate earlier and more completely, reaching a higher final activation fraction of about 90%, as compared to smaller particles. Although smaller soot particles experienced higher actual saturation, their activation/freezing fraction was lower due to their higher equilibrium saturation requirement. The strong size dependence of $\overline{S}_k$ meant that smaller soot particles needed a higher supersaturation to activate, resulting in fewer of them freezing, as compared to larger soot particles.

The instantaneous particle radius fields (shown as scatter) and actual saturation ratio (shown as contours) in a lateral view of the jet

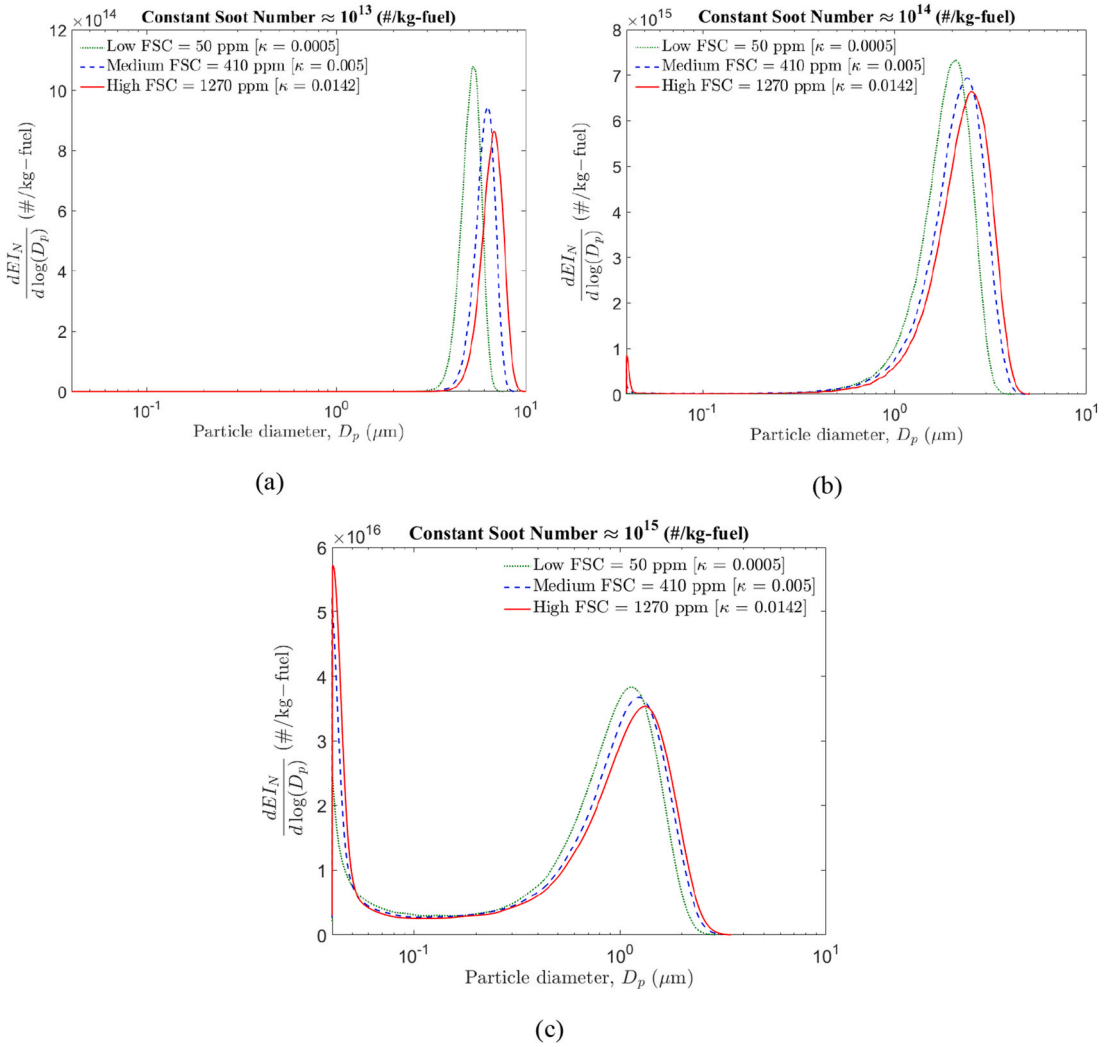

Fig. 8. Particle number emission index distribution $dEI_N/dlog(D_p)$ (1/kg-fuel) as a function of particle diameter for different FSC levels at 1s plume age, with an initial dry soot core radius of 20 nm for all cases, shown for four cases with varying initial soot number emission indices: (a) $EI_{soot} \approx 10^{13}$/kg-fuel, (b) $EI_{soot} \approx 10^{14}$/kg-fuel, and (c) $EI_{soot} \approx 10^{15}$/kg-fuel.

at a plume age of 0.5 s are presented in Fig. 11 for three different initial dry soot core radii: (a) 10 nm, (b) 20 nm, and (c) 30 nm, under a soot emission index of $EI_{soot} \approx 10^{14}$/kg-fuel and a constant low FSC of 50 ppm. The stronger apparent asymmetry in the 10 nm snapshot reflects instantaneous 3D turbulent mixing, not a directional bias from the random particle seeding. The case with the largest initial dry soot core radius at 30 nm shows lower saturation levels (as previously shown in Fig. 9(a)), as faster ice particle growth depletes water vapor more efficiently, reducing local supersaturation and accelerating the plume's thermodynamic equilibration.

3.4. Comparison of 3D online-coupled microphysics and 0D offline box model

In the literature, 0D box models are widely used to investigate contrail formation and evolution, as they allow extensive parametric studies at relatively low computational cost as compared to LES. However, these models neglect strong fluctuations in temperature and saturation profiles, which can lead to significant prediction errors. To complement the 3D LES with κ-Köhler theory, a 0D offline box model is then analyzed to highlight how the resulting microphysics differs from that predicted by the LES.

The conditions were adapted from the Lewellen's baseline case study (Lewellen, 2020), as detailed in Table 3 below:

The simulation was conducted using a monodisperse size distribution for soot particles at initialization, with results presented in Fig. 12(a). A polydisperse inlet was tested but yielded only marginal differences while greatly increasing computational cost, so the monodisperse inlet was retained. The turbulence realization closely matched Lewellen's third turbulence realization, demonstrating excellent agreement between the results. Lewellen's study employed a κ value of 0.005, corresponding to a medium FSC case; thus, three κ, representative of previously defined FSC levels, were examined here. As illustrated in Fig. 12(a), the lower κ value exhibits

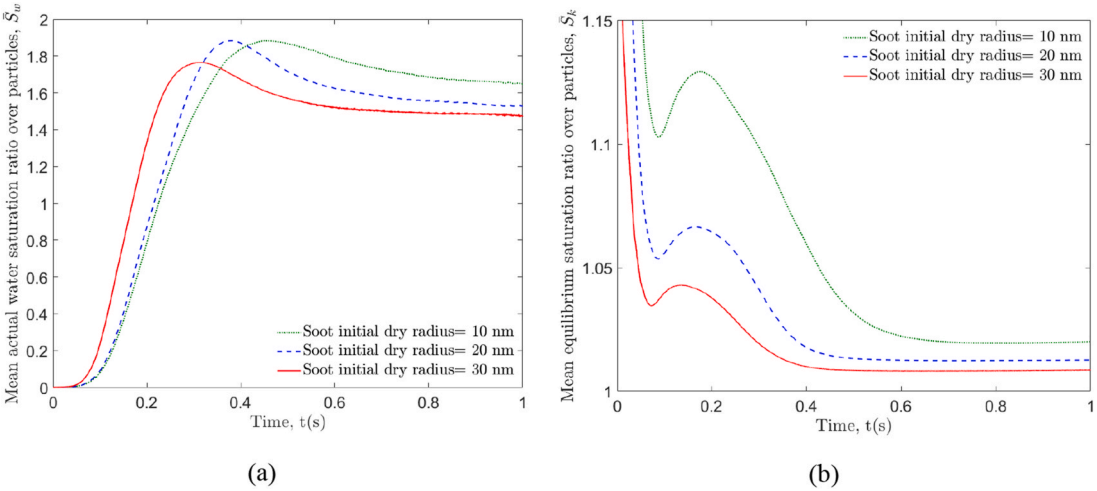

Fig. 9. Temporal evolution of (a) mean actual saturation ratio and (b) mean equilibrium saturation ratio for three initial dry soot core radii of 10 nm, 20 nm, and 30 nm, with a fixed EI_{soot} of 10^{14}/kg-fuel and a low FSC of 50 ppm.

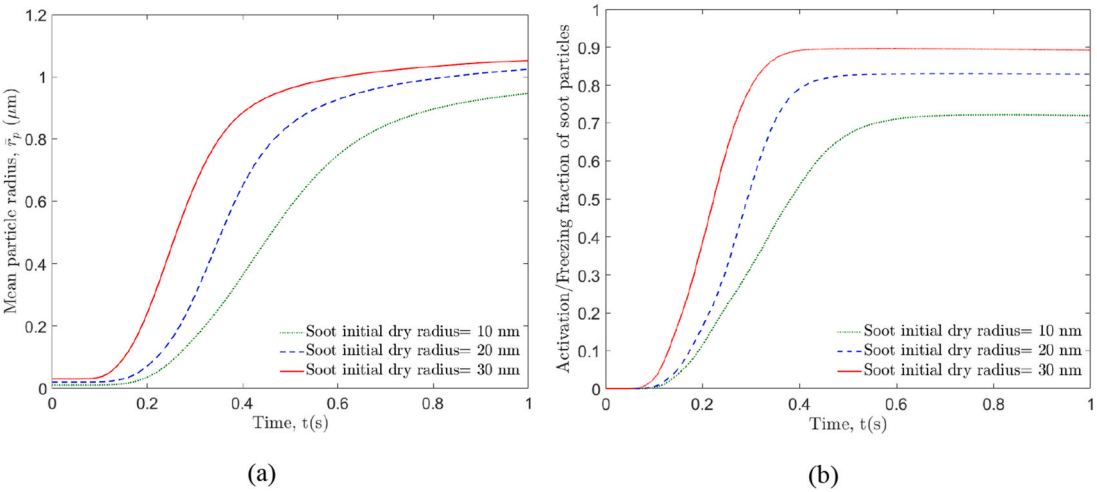

Fig. 10. Temporal evolution of (a) mean soot particle radius and (b) activation/freezing fraction of soot particles for three initial dry soot core radii of 10 nm, 20 nm, and 30 nm, with a fixed EI_{soot} of 10^{14}/kg-fuel and a low FSC of 50 ppm.

slightly higher activation fractions as compared to higher κ values, aligning with expectations and trends previously presented in Fig. 4 (b). Subsequently, the plume-averaged mixing fraction and cooling rate extracted from the 3D simulations were utilized to derive 0D offline results. All equations governing the microphysics of the 0D offline box model were identical to those implemented in the FludiLES code, as outlined in **Section 2.2**.

Fig. 12(b) illustrates a contrasting trend between offline and online simulations, wherein the higher κ value exhibits marginally greater activation fractions than the lower κ value. Moreover, the offline model overpredicts the total ice number because it cannot account for vapor-sink feedback and inter-parcel mixing, which in the online simulation, suppress later activation and cause deactivation of droplets. This comparison underscores the significance of 3D online coupling, especially concerning sensitive parameters like κ, which critically influence the activation behavior.

These findings align with those of Bier et al. (Bier et al., 2022), who showed that neither ensemble trajectories offline from an LES nor a single averaged trajectory from a box model can capture online microphysical feedback, leading to overpredictions of ice number relative to a fully coupled 3D LES. Their κ-Köhler analysis also indicated that lower κ slightly reduces activation fractions—consistent with our 0D offline box-model trend (Fig. 12(b)), while the particle-resolving approach captures fluctuation-driven mixing and vapor-sink feedbacks.

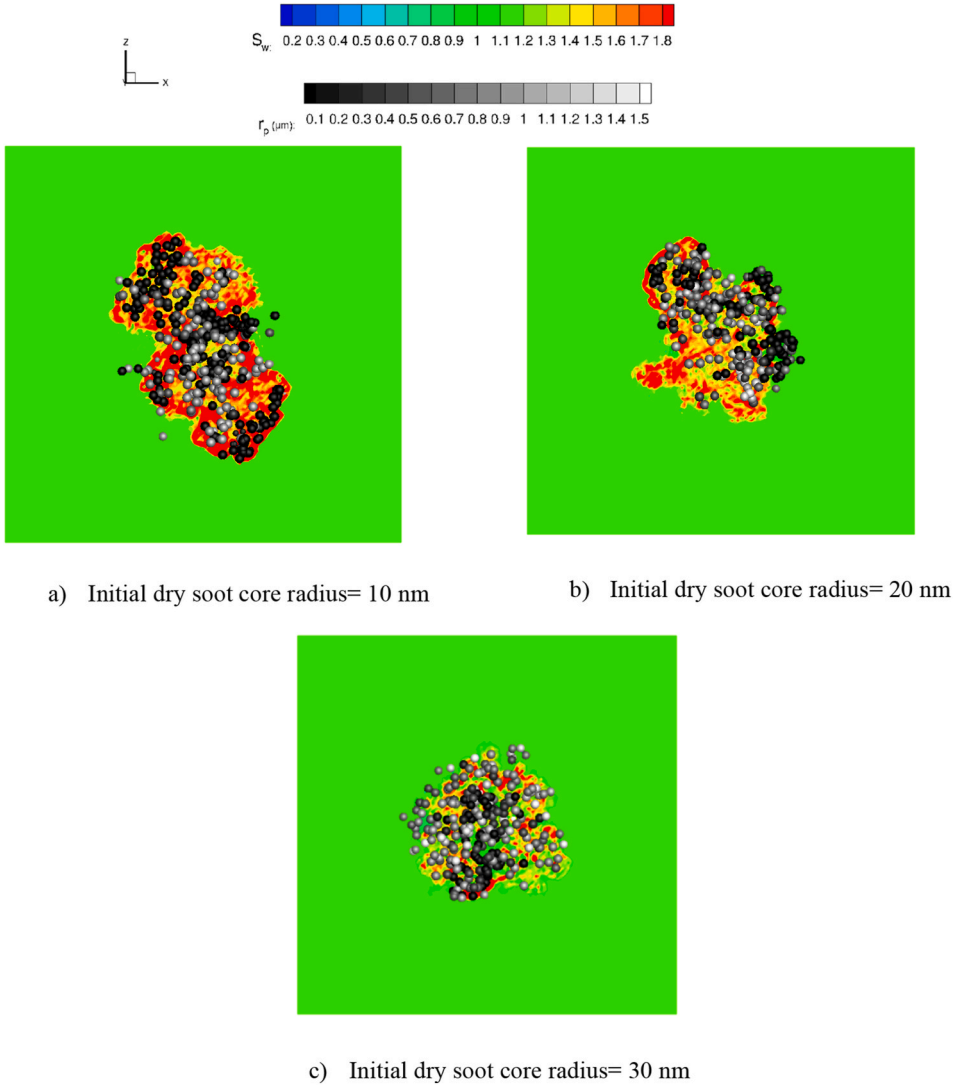

Fig. 11. Distribution of particle radius (scatter) and actual saturation field (contours) in the lateral view of the exhaust plume at a plume age of 0.5s for three different initial dry soot core radii: (a) 10 nm, (b) 20 nm, and (c) 30 nm, with a fixed EI_{soot} of 10^{14}/kg-fuel and a low FSC of 50 ppm. Particle radius is encoded only by color (darker = smaller). (For interpretation of the references to color in this figure legend, the reader is referred to the Web version of this article.)

Table 3
Baseline Simulation Parameters from Lewellen (Lewellen, 2020) study.

Parameters	Values
Specific Combustion Heat (J.kg^{-1})	4.29×10^7
Overall Propulsion Efficiency	0.325
Exhaust Jet Temperature (K)	480
Initial plume dilution	92
Initial Plume Cross-Sectional Area (m^2)	0.31
Water Vapor Mass Emission Index (kg-w/kg-fuel)	1.25
Soot Number Emission Index (#1/kg-fuel)	10^{16}
Dry Core Radius of Soot Particles (nm)	20
Soot Particle Hygroscopicity (κ)	0.005
Ambient Temperature (K)	218.8
Ice Relative Humidity	110%
Ambient Pressure (Pa)	23840

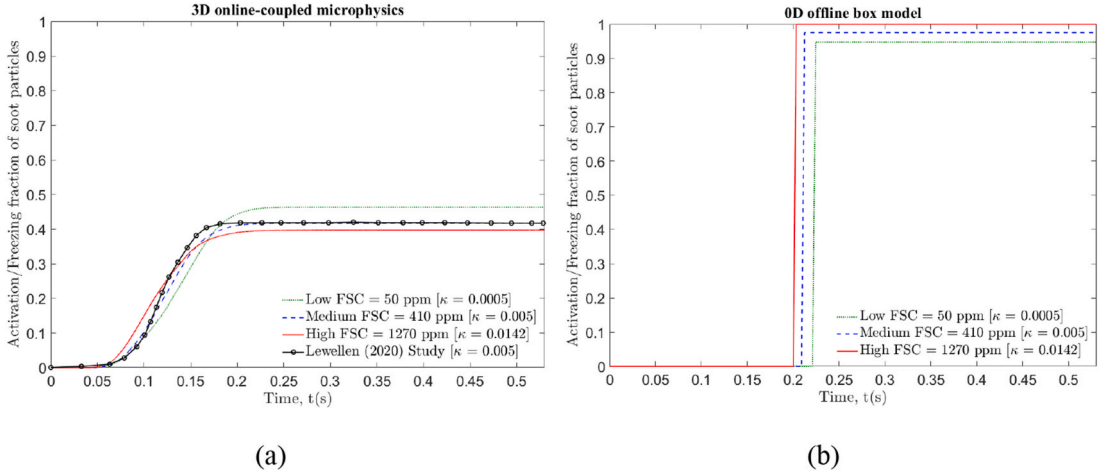

Fig. 12. Comparison of a) 3D online-coupled microphysics and b) 0D Offline box model for the Lewellen (Lewellen, 2020) Baseline case at three FSC Levels: low FSC = 50 ppm, medium FSC = 410 ppm, and high FSC = 1270 ppm.

4. Conclusion

This study investigates the effects of the soot particle hygroscopicity, soot emission indices (EI_{soot}), and initial soot core radius on the formation and growth of ice crystals in aircraft contrails. A refined microphysical model for soot activation, coupled online with LES, was developed to simulate the near-field evolution of exhaust plumes from a LEAP-1A engine under realistic cruise conditions. The model explicitly accounted for solute effects by representing water activity through the hygroscopicity parameter, capturing the influence of sulfuric acid coatings on soot particle activation and growth. Numerical simulations were performed up to 1s plume age, corresponding to the jet regime, where soot particle activation predominantly occurs.

The following is a summary of the key findings from the study:

1. Variations in the hygroscopicity parameter (κ), linked to FSC levels (low, medium and high), influenced both the ice particle size and activation behavior. Increasing κ (or FSC) produced larger mean ice particle radii but reduced activation fractions. Such trends occurred under conditions where soot particles alone contributed to microphysical processes: a higher FSC enhanced the growth of already activated particles, depleting available water vapor, thereby hindering further activation. The results highlighted the complex interplay between sulfur-driven water vapor dynamics and soot particle activation.
2. Variations in EI_{soot} significantly influenced the microphysical properties of soot-derived ice particles. A lower EI_{soot} substantially increased both the mean ice particle radius and activation fraction, resulting in more uniform particle size distributions. These results underscored the importance of accurately representing EI_{soot}, as variations affect soot particle activation, growth, and size distribution—key factors governing subsequent contrail development.
3. Variations in the initial soot core radius along with increasing size produced larger mean ice particle sizes and higher activation fractions. In contrast, smaller soot core radii, being more resistant to activation due to the Kelvin effect, resulted in both lower ice particle sizes and reduced activation fractions. These results indicate that the initial soot core radius, as a key determinant of particle size at activation, should be explicitly parameterized in contrail microphysics.
4. Comparisons of the 0D offline box model with 3D online-coupled microphysics revealed differences in the sensitivity of activation fractions to κ. These fractions were notably higher in the 0D offline box model, primarily as a result of using a single mean value per time step, which alters the κ sensitivity. The 0D offline box model exhibited an opposing trend, with slightly higher activation fractions at elevated κ values than at lower ones. By contrast, the 3D online-coupled microphysics, which resolves vapor uptake for each individual soot particle, consistently produced lower activation fractions for higher κ values during the initial stages of the plume. This comparison underscored the need for 3D online-coupled microphysics when parameterizing sensitive variables such as κ, owing to the nonlinear behavior inherent in the κ-Köhler theory.

The study underscores the importance of detailed and accurate modeling of activation processes, as they strongly influence the soot-derived ice particle number and size distributions starting from the earliest stages of exhaust plume development, with implications for subsequent plume evolution. Future work could extend this research by incorporating additional particle types, such as volatile and organic particles, to assess their contributions, particularly in scenarios involving SAFs with very low soot emission indices, which were not considered herein. Moreover, future investigations should examine downstream plume evolution into the vortex phase to provide a more comprehensive understanding of contrail dynamics.

CRediT authorship contribution statement

Parisa Afkari: Writing – review & editing, Writing – original draft, Visualization, Validation, Software, Methodology, Investigation, Formal analysis, Data curation, Conceptualization. **Mohamed Chouak:** Writing – review & editing, Writing – original draft, Project administration, Investigation, Conceptualization. **Sébastien Cantin:** Writing – review & editing, Writing – original draft, Project administration, Investigation. **François Garnier:** Writing – review & editing, Supervision, Resources, Funding acquisition.

Declaration of competing interest

The authors declare that they have no known competing financial interests or personal relationships that could have appeared to influence the work reported in this paper.

Acknowledgment

This research was enabled in part by support provided by the Calcul Québec (calculquebec.ca) and the Digital Research Alliance of Canada (alliancecan.ca).

Data availability

Data will be made available on request.

References

Afkari, P., Chouak, M., Cantin, S., & Garnier, F. (2025). Evaluating bypass effects of advanced turbofan engines on contrail formation using large eddy simulations. *Journal of Aircraft*, 1–14.

Appleman, H. (1953). The formation of exhaust condensation trails by jet aircraft. *Bulletin of the American Meteorological Society, 34*(1), 14–20.

Bier, A., Unterstrasser, S., & Vancassel, X. (2022). Box model trajectory studies of contrail formation using a particle-based cloud microphysics scheme. *Atmospheric Chemistry and Physics, 22*(2), 823–845.

Bräuer, T., Voigt, C., Sauer, D., Kaufmann, S., Hahn, V., Scheibe, M., Schlager, H., Huber, F., Le Clercq, P., Moore, R. H., & Anderson, B. E. (2021). Reduced ice number concentrations in contrails from low-aromatic biofuel blends. *Atmospheric Chemistry and Physics, 21*(22), 16817–16826.

Brunet, S., Garnier, F., & Sagaut, P. (1999). Crow instability effects on the exhaust plume mixing and condensation. In *ESAIM: Proceedings*. EDP Sciences.

Cantin, S., Chouak, M., & Garnier, F. (2025). Effects of fuel sulfur content and nvPM emissions on contrail formation: A CFD–microphysics study including the role of organic compounds. *Journal of Aerosol Science*, Article 106612.

Celik, I. B., Ghia, U., Roache, P. J., & Freitas, C. J. (2008). Procedure for estimation and reporting of uncertainty due to discretization in CFD applications. *Journal of fluids Engineering-Transactions of the ASME, 130*(7).

DeVries, P., DeVries, P. L., & Hasbun, J. (2011). *A first course in computational physics*. Jones & Bartlett Learning.

Fukuta, N., & Walter, L. (1970). Kinetics of hydrometeor growth from a vapor-spherical model. *Journal of the Atmospheric Sciences, 27*(8), 1160–1172.

Gago, C. F., Brunet, S., & Garnier, F. (2002). Numerical investigation of turbulent mixing in a jet/wake vortex interaction. *AIAA Journal, 40*(2), 276–284.

Gago, C. F., Garnier, F., & Utheza, F. (2003). Direct testing of subgrid scale models in large-eddy simulation of a non-isothermal turbulent jet. *International Journal for Numerical Methods in Fluids, 42*(9), 999–1026.

Garnier, F., Brunet, S., & Jacquin, L. (1997). Modelling exhaust plume mixing in the near field of an aircraft. In *Annales geophysicae*. Copernicus GmbH.

Garnier, F., Gago, C. F., Brasseur, A. L., Paoli, R., & Cuenot, B. (2003). Dispersion and growing of ice particles in a turbulent exhaust plume. In *European Conference on Aviation, Atmosphere and Climate*.

Garnier, F., Maglaras, E., Morency, F., & Vancassel, X. (2014). Effect of compressibility on contrail ice particle growth in an engine jet. *International Journal of Turbo & Jet-Engines, 31*(2), 131–140.

Iata, I. A. T. A. (2024). *Aviation contrails and their climate effect (tackling uncertainties and enabling solutions)*. Report. Available from: https://www.iata.org/contentassets/726b8a2559ad48fe9decb6f2534549a6/aviation-contrails-climate-impact-report.pdf.

ICAO. (2024). Aircraft engine emissions databank [Available from: https://www.easa.europa.eu/en/domains/environment/icao-aircraft-engine-emissions-databank.

Kärcher, B. (2016). The importance of contrail ice formation for mitigating the climate impact of aviation. *Journal of Geophysical Research: Atmospheres, 121*(7), 3497–3505.

Kärcher, B. (2018). Formation and radiative forcing of contrail cirrus. *Nature Communications, 9*(1), 1–17.

Kärcher, B., Burkhardt, U., Bier, A., Bock, L., & Ford, I. J. (2015). The microphysical pathway to contrail formation. *Journal of Geophysical Research: Atmospheres, 120*(15), 7893–7927.

Kärcher, B., & Yu, F. (2009). Role of aircraft soot emissions in contrail formation. *Geophysical Research Letters, 36*(1).

Khou, J. C., Ghedhaifi, W., Vancassel, X., & Garnier, F. (2015). Spatial simulation of contrail formation in near-field of commercial aircraft. *Journal of Aircraft, 52*(6), 1927–1938.

Khou, J. C., Ghedhaïfi, W., Vancassel, X., Montreuil, E., & Garnier, F. (2017). CFD simulation of contrail formation in the near field of a commercial aircraft: Effect of fuel sulfur content. *Meteorologische Zeitschrift, 26*(6), 585–596.

Labbe, O., Maglaras, E., & Garnier, F. (2007). Large-eddy simulation of a turbulent jet and wake vortex interaction. *Computers & Fluids, 36*(4), 772–785.

Lele, S. K. (1992). Compact finite difference schemes with spectral-like resolution. *Journal of Computational Physics, 103*(1), 16–42.

Lewellen, D. C. (2020). A large-eddy simulation study of contrail ice number formation. *Journal of the Atmospheric Sciences, 77*(7), 2585–2604.

Li, Y. Q., Davidovits, P., Kolb, C. E., & Worsnop, D. R. (2001). Mass and thermal accommodation coefficients of H2O (g) on liquid water as a function of temperature. *The Journal of Physical Chemistry A, 105*(47), 10627–10634.

Maglaras, E. (2007). *Application de la Simulation Numérique des Grandes Échelles à la Formation des Traînées de Condensation dans le Sillage d'un Avionn*. Bordeaux 1.

Mozurkewich, M. (1986). Aerosol growth and the condensation coefficient for water: A review. *Aerosol Science and Technology, 5*(2), 223–236.

Murphy, D. M., & Koop, T. (2005). Review of the vapour pressures of ice and supercooled water for atmospheric applications. *Quarterly Journal of the Royal Meteorological Society: A Journal of the Atmospheric Sciences, Applied Meteorology and Physical Oceanography, 131*(608), 1539–1565.

Panda, J., Zaman, K., & Seasholtz, R. (2004). Measurements of initial conditions at nozzle exit of high-speed jets. In *7th AIAA/CEAS aeroacoustics conference and exhibit*.

Paoli, R., Vancassel, X., Garnier, F., & Mirabel, P. (2008). Large-eddy simulation of a turbulent jet and a vortex sheet interaction: particle formation and evolution in the near field of an aircraft wake. *Meteorologische Zeitschrift, 17*(2), 131–144.

Paoli, R., Nybelen, L., Picot, J., & Cariolle, D. (2013). Effects of jet/vortex interaction on contrail formation in supersaturated conditions. *Physics of Fluids, 25*(5).

Paoli, R., & Garnier, F. (2005). Interaction of exhaust jets and aircraft wake vortices: Small-scale dynamics and potential microphysical-chemical transformations. *Comptes Rendus Physique, 6*(4-5), 525–547.
Petters, M., & Kreidenweis, S. (2007). A single parameter representation of hygroscopic growth and cloud condensation nucleus activity. *Atmospheric Chemistry and Physics, 7*(8), 1961–1971.
Petzold, A., Gysel, M., Vancassel, X., Hitzenberger, R., Puxbaum, H., Vrochticky, S., Weingartner, E., Baltensperger, U., & Mirabel, P. (2005). On the effects of organic matter and sulphur-containing compounds on the CCN activation of combustion particles. *Atmospheric Chemistry and Physics, 5*(12), 3187–3203.
Popovicheva, O., Persiantseva, N. M., Shonija, N. K., DeMott, P., Koehler, K., Petters, M., Kreidenweis b, S., Tishkova c, V., Demirdjian, B., & Suzanne, J. (2008). Water interaction with hydrophobic and hydrophilic soot particles. *Physical Chemistry Chemical Physics, 10*(17), 2332–2344.
Pruppacher, H. R., & Klett, J. D. (1979). *Microphysics of clouds and precipitation*. Dordrecht: Reidel.
Riechers, B., Wittbracht, F., Hütten, A., & Koop, T. (2013). The homogeneous ice nucleation rate of water droplets produced in a microfluidic device and the role of temperature uncertainty. *Physical Chemistry Chemical Physics, 15*(16), 5873–5887.
Schmidt, E. (1941). Die Entstehung von Eisnebel aus den Auspuffgasen von Flugmotoren. *Schriften der Deutschen Akademie der Luftfahrtforschung, 5*(44), 1–15. Verlag R. Oldenbourg, München, Heft 44.
Schumann, U. (1996). On conditions for contrail formation from aircraft exhausts. *Meteorologische Zeitschrift, 5*, 4–23.
Schumann, U., Ström, J., Busen, R., Baumann, R., Gierens, K., Krautstrunk, M., Schröder, F. P., & Stingl, J. (1996). In situ observations of particles in jet aircraft exhausts and contrails for different sulfur-containing fuels. *Journal of Geophysical Research: Atmospheres, 101*(D3), 6853–6869.
Schumann, U., Arnold, F., Busen, R., Curtius, J., Kärcher, B., Kiendler, A., Petzold, A., Schlager, H., Schröder, F., & Wohlfrom, K. H. (2002). Influence of fuel sulfur on the composition of aircraft exhaust plumes: The experiments SULFUR 1–7. *Journal of Geophysical Research: Atmospheres, 107*(D15). AAC-2.
Singh, D. K., Sanyal, S., & Wuebbles, D. J. (2024). Understanding the role of contrails and contrail cirrus in climate change: A global perspective. *Atmospheric Chemistry and Physics, 24*(16), 9219–9262.
Vancassel, X., Mirabel, P., & Garnier, F. (2014). Numerical simulation of aerosols in an aircraft wake using a 3D LES solver and a detailed microphysical model. *International Journal of Sustainable Aviation, 1*(2), 139–159.
Vichnevetsky, R., & Bowles, J. B. (1982). *Fourier analysis of numerical approximations of hyperbolic equations*. SIAM.
Voigt, C., Kleine, J., Sauer, D., Moore, R. H., Bräuer, T., Le Clercq, P., Kaufmann, S., Scheibe, M., Jurkat-Witschas, T., Aigner, M., Bauder, U., Boose, Y., Borrmann, S., Crosbie, E., Diskin, G. S., DiGangi, J., Hahn, V., Heckl, CH., Huber, F., et al. (2021). Cleaner burning aviation fuels can reduce contrail cloudiness. *Communications Earth & Environment, 2*(1), 114.
Wong, H.-W., & Miake-Lye, R. (2010). Parametric studies of contrail ice particle formation in jet regime using microphysical parcel modeling. *Atmospheric Chemistry and Physics, 10*(7), 3261–3272.
Yu, F., Karcher, B., & Anderson, B. E. (2024). Revisiting contrail ice formation: Impact of primary soot particle sizes and contribution of volatile particles. *Environmental Science and Technology, 58*(40), 17650–17660.